Journal of Alloys and Compounds 844 (2020) 156014

Contents lists available at ScienceDirect

Journal of Alloys and Compounds

journal homepage: http://www.elsevier.com/locate/jalcom

In-situ visualization of corrosion behavior of $Al_xCoCrFeNi$ high-entropy alloys during electrochemical polarization

Yunzhu Shi [a], Jingke Mo [b, c], Feng-Yuan Zhang [c], Bin Yang [d], Peter K. Liaw [e, **], Ying Zhao [a, *]

[a] Shenzhen Institutes of Advanced Technology, Chinese Academy of Sciences, Shenzhen, 518055, China
[b] Department of Aeronautics and Astronautics, Fudan University, Shanghai, 200433, China
[c] Department of Mechanical, Aerospace & Biomedical Engineering, UT Space Institute, The University of Tennessee, Tullahoma, TN 37388, USA
[d] Collaborative Innovation Center of Steel Technology, University of Science and Technology Beijing, Beijing, 100083, China
[e] Department of Materials Science and Engineering, The University of Tennessee, Knoxville, TN 37996, USA

ARTICLE INFO

Article history:
Received 13 March 2020
Received in revised form
26 April 2020
Accepted 8 June 2020
Available online 24 June 2020

Keywords:
High-entropy alloys
Corrosion
Microstructure
In-situ visualization
Metastable pitting

ABSTRACT

In the present study, the corrosion behavior of the $Al_xCoCrFeNi$ (x = 0.3, 0.5, 0.7) high-entropy alloys (HEAs) is investigated by an in-situ visualization system. Surface morphology changes on both micro-spatial and temporal scales are monitored in the 3.5 wt% NaCl solution during the potentiodynamic polarization. The microstructures of the $Al_xCoCrFeNi$ HEAs are characterized by SEM, EBSD, and EDS. The results show that the microstructure evolves from singe face-centered cubic (FCC) phase to multi-phases by increasing the Al content. The in-situ observations directly reveal the different localized corrosion processes in the $Al_xCoCrFeNi$ HEAs. In the single FCC phase $Al_{0.3}CoCrFeNi$ HEA, localized corrosion shows in the form of pitting. In the $Al_{0.5}CoCrFeNi$ and $Al_{0.7}CoCrFeNi$ alloys, which possess FCC and body-centered cubic (BCC) phases, the localized corrosion initiates and propagates in the Cr-depleted BCC phase. In addition, the in-situ visualization uncovers the evolution of current serration, which represents the propagation and repassivation of metastable pit during the polarization. The frequent occurrence of metastable pits indicates distinct repassivation ability of the $Al_{0.3}CoCrFeNi$ HEA.

1. Introduction

By breaking the traditional alloy-design principle, high-entropy alloys (HEAs) that contain five or more principal elements in equal or near-equal atomic percent (at.%) were developed [1,2]. Because of the high mixing entropy effect, HEAs favor the formation of one or more solid solutions instead of intermetallics [3–7]. HEAs are being seen as potential candidates for a number of engineering applications because that they have shown several attractive properties, including good strength-ductility [8,9], high thermal-stability [10], and good wear resistance [11]. Besides, HEAs perform an outstanding corrosion resistance, due to the high concentration and homogeneous distribution of passivating elements, especially for the HEAs that possess the single-solid solution phase [12]. However, like other passive-film-forming alloys, which are designed to be corrosion-resistant, HEAs can nevertheless undergo localized corrosion, which is one of the most detrimental and undetectable forms of corrosion and rapidly leads to the failure.

Due to the small size and the fact that it may be hidden under a concealed area, localized corrosion is more destructive than general corrosion. Localized corrosion usually occurs in the forms of pitting, selective dissolution, crevice corrosion, etc. In the previous study, the addition of Al to the CoCrFeNi alloy could improve the tensile strength [13]. However, because of the formation Al–Ni rich secondary phase, the alloy is more susceptible to localized corrosion [14]. Since the localized corrosion is more likely to nucleate at the local site where the passive film is relatively weak, the morphology, distribution, and volume fraction of the active sites are determinant facts of the corrosion processes. Efforts have been made to study the relationship between microstructure and localized corrosion behavior of HEAs. For example, in the case of the as-cast AlCoCrFeNi alloy [15], Cr segregation occurs in interdendritic regions. The Cr-depleted dendrites suffer from the selective corrosion in a 0.6 M NaCl solution. However, the localized corrosion processes are usually speculated based on the surface morphologies afterwards. Beside, during the potentiodynamic polarization of HEAs, current

* Corresponding author.
** Corresponding author.
E-mail addresses: yz.shi1@siat.ac.cn (Y. Shi), jkmo@fudan.edu.cn (J. Mo), fzhang9@utk.edu (F.-Y. Zhang), byang@ustb.edu.cn (B. Yang), pliaw@utk.edu (P.K. Liaw), ying.zhao@siat.ac.cn (Y. Zhao).

https://doi.org/10.1016/j.jallcom.2020.156014
0925-8388/

serrations, which represent the formation and evolution of metastable pits, have often been detected before reaching the breakdown potential [16,17]. As the precursor of pitting, metastable pitting plays an important role in the corrosion process. Due to the limitation of observation method, the real-time metastable pitting process during the polarizations of HEAs remains unknown, thus, calling for direct experimental evidence for an in-depth understanding.

In the present study, the localized corrosion and metastable pitting processes of $Al_xCoCrFeNi$ HEAs are firstly revealed in-situ by an advanced visualization system coupled with electrochemical polarization. The microstructure is characterized by scanning electron microscopy (SEM), energy-dispersive X-ray spectroscopy (EDS), and electron back-scattered diffraction (EBSD). The surface morphology changes of the $Al_xCoCrFeNi$ HEAs on both micro-spatial and temporal scales under the electrochemical control are monitored to provide direct experimental results for a better understanding of localized corrosion process and metastable pitting behavior. This measurement opens up a new scope for understanding the corrosion mechanism through the in-situ observation of localized corrosion and repassivation processes.

2. Material and methods

2.1. Test materials

Al, Co, Cr, Fe, and Ni metals of high purity (99.99 wt %) were used as raw materials for the preparation of the as-cast $Al_xCoCrFeNi$ alloy [atom ratios of Al/(CoCrFeNi) are $x/(1+1+1+1)$, with $x = 0.3$, 0.5, and 0.7]. The raw materials were fabricated by repeated arc-melting and casting under vacuum (0.01 atm) for at least 5 times to improve the chemical homogeneity. The specimens for the SEM/EBSD study were cut as cubic samples with a size of 10 mm × 10 mm × 5 mm, then wet ground with SiC papers up to 2000 grit and mechanically polished using a 0.5 μm diamond paste. The samples for the common potentiodynamic polarization tests were cut as 10 mm × 10 mm × 5 mm cubic, and cold-mounted in epoxy with copper lines spot-welded on the back for the electrical contact. The test surface (with an area of 1 cm^2) was wet ground with SiC papers up to 2000 grit, cleaned thoroughly with acetone, alcohol, and deionized water in sequence, and then dried with the flowing compressed hot air.

2.2. Microstructure and chemical analysis

The microstructure of the $Al_xCoCrFeNi$ HEAs were observed using a LEO Gemini 1525 field-emission scanning-electron microscope (SEM, ZEISS SUPRA 55) operated at 20 kV, with the equipped backscattering-electron detector (BSE, K. E. Developments Ltd. Cambridge, UK). The phase compositions were detected by EDS linked to the SEM system. Electron backscattered diffraction detector (EBSD, Bruker) installed in the ZEISS Auriga system was operated at 20 kV and analyzed by the TSL OIM Analysis software to determine the crystal type of each phase.

2.3. Electrochemical measurements

The potentiodynamic polarizations were carried out using the Potentiostat Workstation PARSTAT 2263, with a three-electrode electrochemical cell. A saturated calomel electrode (SCE) was used as the reference electrode. A platinum sheet was employed as the auxiliary electrode, and a specimen as the working electrode. The electrochemical measurements were performed at room temperature (20 ± 2 °C) in the 3.5 wt% NaCl solution. Before the potentiodynamic polarizations, the samples were immersed and allowed to corrode freely for at least 30 min to reach a quasi-stationary value of the open circuit potential (OCP). The potentiodynamic-polarization tests were performed at a scan rate of 1 mV/s from an initial potential of − 0.25 V vs. OCP. To confirm data reproducibility, the polarization tests were performed at least three times.

2.4. In-situ visualization test

Surface morphology observations were conducted using an in-situ visualization system, which consisted of a high-speed camera (Phantom V711) and in-house optical assembly [18]. The high-speed camera can achieve a maximum speed of 7500 frames-per-second at full resolution. The in-house optical assembly was composed of a main zoom lens body and a series of objective and eye-piece lenses, with a working distance of >70 mm even at high resolution [19,20]. The visualization system continuously captured images of the sample surface during the potentiodynamic polarization tests at 0.01 s intervals. It should be noticed that the exposed surface area of the working electrode for the in-situ visualization test was smaller than that for the common electrochemical test, which was necessary that the images captured by video microscope contain the entire test area. The small test area also reduced the frequency of occurrence of metastable pit nucleation, avoiding any overlap of the current transients and allowing them to be separated in time. The schematic diagram of the visualization system coupled with the electrochemical measurement is shown in Fig. 1.

3. Results

3.1. Microstructure characterizations

The microstructures of the $Al_xCoCrFeNi$ HEAs are shown in Fig. 2, as revealed by the back-scattered-electron (BSE) images and EBSD phase map. The microstructure of the $Al_{0.3}CoCrFeNi$ alloy appears as a single face-centered cubic (FCC) phase according to Fig. 2a, d. No contrast variation is observed in BSE images (Fig. 2a), indicating that elements are distributed homogeneously in the FCC solid solution. The detailed compositions detected by EDS are listed in Table 1. For the $Al_{0.5}CoCrFeNi$ alloy, the BSE image (Fig. 2b) shows two phases with contrast variation. One is the light-gray matrix and the other is the dark-gray precipitate which distributes dispersedly. The EBSD phase map (Fig. 2e) indicates that the light-gray matrix is FCC phase and the crystal-structure of the precipitate is BCC. The EDS results shown in Table 1 reveal that the FCC phase is Fe and Cr-rich. In contrasts, the BCC precipitate is enriched with Al and Ni. With the further increase of Al content, the microstructure changes significantly in the $Al_{0.7}CoCrFeNi$ HEA, as shown in Fig. 2c, f The

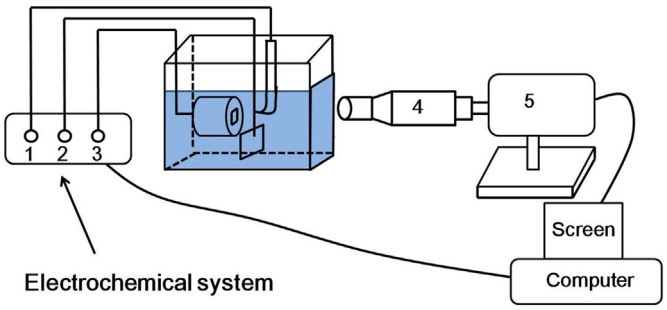

Fig. 1. Schematic diagram of in-situ visualization test system: (1) reference electrode, (2) auxiliary electrode, (3) working electrode, (4) optical assembly, (5) high-speed camera.

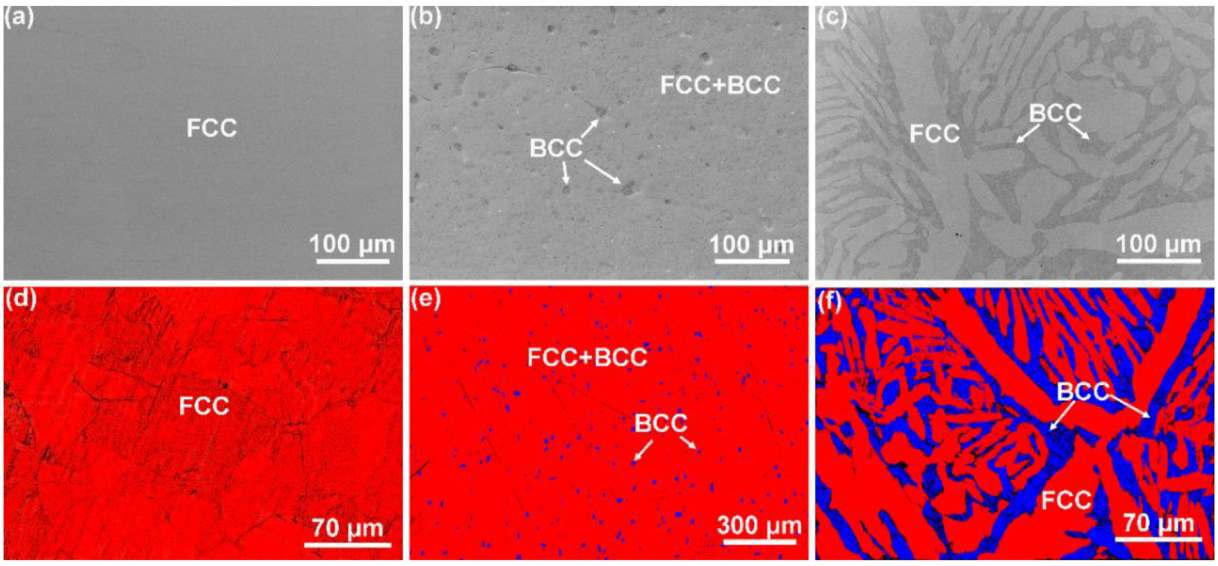

Fig. 2. Backscattered-electron (BSE) images (a–c), and electron-backscattered diffraction (EBSD) phase maps (d–f) of $Al_{0.3}$CoCrFeNi (a, d), $Al_{0.5}$CoCrFeNi (b, e), and $Al_{0.7}$CoCrFeNi (c, f).

Table 1
EDS-analysis results for chemical compositions (at.%) of Al_xCoCrFeNi alloys. Values within parenthesis are standard deviations.

Alloys	Phases	Al	Co	Cr	Fe	Ni
$Al_{0.3}$CoCrFeNi	FCC	7.0 (±0.1)	23.2 (±0.1)	23.4(±0.1)	23.4(±0.2)	23.0 (±0.2)
$Al_{0.5}$CoCrFeNi	FCC	10.6 (±0.7)	22.3 (±0.7)	22.9(±0.4)	22.7(±0.4)	21.4 (±0.8)
	BCC	24.3 (±0.2)	18.5 (±0.1)	13.0 (±0.2)	14.7(±0.1)	29.5(±0.1)
$Al_{0.7}$CoCrFeNi	FCC	10.3(±0.1)	22.7 (±0.2)	22.4 (±0.2)	22.6 (±0.5)	19.0(±1.0)
	BCC	21.9(±0.2)	19.5(±0.1)	16.9 (±0.1)	17.2 (±0.2)	24.3(±1.2)

volume fraction of the BCC phase has increased dramatically, and the microstructure consists of dendrites (FCC phase) and interdendrites (BCC phase). Similar to the $Al_{0.5}$CoCrFeNi alloy, the FCC phase is enriched with Fe and Cr, and the BCC phase is Al and Ni-rich (Table 1). The formation of the Al-rich BCC phase with the increased Al content is caused by the increased lattice distortion energy induced by the Al addition in the closed-packed FCC structure. Since the Al has a larger atomic radius than the other elements, the transition from the FCC to BCC crystal-structure could relax the lattice-distortion energy [13].

3.2. Potentiodynamic-polarization

The potentiodynamic-polarization curves of the Al_xCoCrFeNi HEAs samples detected in the 3.5 wt% NaCl solution at room temperature with the scan rate of 1 mV/s are shown in Fig. 3. The exposed areas of the samples are 1 cm^2. The three curves show the obviously passive region, indicating stable oxide films have formed. The current density in the passive region (I_{pass}) is on the order of 10^{-4} mA/cm^2, revealing that the ionic transport rate through the oxide film is low, thus resisting the corrosion. With the increase of applied potential, the passive film breaks after reaching the breakdown potential (E_b), where the current density dramatically increases. As shown in Fig. 3, the E_b decreases with the increased Al content, demonstrating that the sustained breakdown of passive film is easier to happen and the resistance to localized corrosion decreases. Before reaching the E_b, current fluctuations occur, which indicate the nucleation, growth, and repassivation of metastable pits [21]. During the polarization, in-situ visualization tests are performed to monitor morphology changes on both micro-spatial and temporal scales. The localized dissolution behavior and metastable pitting process of the Al_xCoCrFeNi ($x = 0.3$, 0.5, and 0.7) HEAs would be directly revealed. To be noticed, the metastable pitting events often occur with high frequency. This frequency is naturally reduced when the surface area is small. Therefore, during the in-situ visualization test, to allow individual metastable pit to be

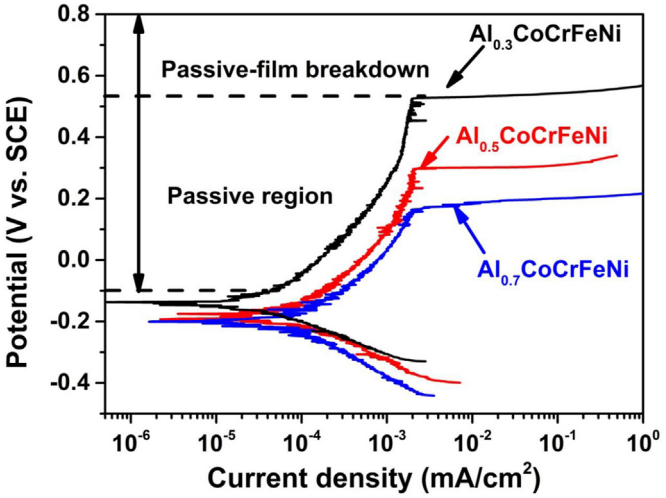

Fig. 3. Potentiodynamic-polarization curves of Al_xCoCrFeNi ($x = 0.3$, 0.5, and 0.7) HEAs with a scan rate of 1 mV/s in the 3.5 wt% NaCl solution at room temperature. The passive region and passive-film breakdown region of the $Al_{0.3}$CoCrFeNi curve are defined.

identified, separated, and analyzed, the exposed area of the working electrode for the in-situ visualization test is much smaller than the common test.

3.3. In-situ visualizations

The morphologies of the $Al_{0.3}CoCrFeNi$ sample surface exposed in the 3.5 wt % NaCl solution at room temperature during the potentiodynamic polarization test were captured in-situ by the micro-scale visualization system. The video obtained during the polarization test under the potential scan rate of 1 mV/s is provided in the supplementary Video S1. Fig. 4a shows the potentiodynamic polarization curve. A stable passive region can be clearly seen. Before reaching the breakdown potential, the current serrations, which represent the formation and repassivation of metastable pits could be observed. Fig. 4b presents the enlarged current fluctuations from 0.4 V to 0.6 V vs. SCE. Several current fluctuations could be detected with the current peaks showing a slow rise and sudden decay. Fig. 4c shows the surface morphology captured at OCP, the surface is smooth without obvious defects. The image captured at the potential of 0.6 V vs. SCE is shown in Fig. 4d. The semi-sphere pits are sparsely formed in the single FCC phase. It reveals that localized corrosion in the $Al_{0.3}CoCrFeNi$ HEA processes in the form of pitting. The marked two pits in Fig. 4d can correspond to the current serrations marked in Fig. 4b (metastable pits 1 and 2) according to the in-situ observation. Due to the relatively small current density of others current spikes and the limited resolution of the visualization system, the metastable pitting behavior corresponding to the relatively small fluctuations cannot be detected clearly. The detailed evolution of the observed metastable pits with time would be analyzed in the section of discussion.

Supplementary video related to this article can be found at https://doi.org/10.1016/j.jallcom.2020.156014.

For the $Al_{0.5}CoCrFeNi$ HEA, Fig. 5a shows the potentiodynamic-polarization curve obtained under the potential scan rate of 1 mV/s. The changes of the surface morphology during the polarization test were captured in-situ and provided in the supplementary Video S2. The polarization curve in Fig. 5a indicates the formation of a stable passive film. Current serrations can be seen as well before reaching the breakdown potential. However, compared to the $Al_{0.3}CoCrFeNi$ HEA, the number of the current spikes is less, as presented in Fig. 5b. Moreover, the current densities of the serration peaks are much small, which are on the order of 10^{-3} mA/cm^2. Due to the small current density, the surface morphology changes corresponding to the current fluctuations cannot be detected in $Al_{0.5}CoCrFeNi$ HEA. Fig. 5c shows the micrograph captured at OCP. Due to the different mechanical properties between the FCC matrix and the BCC precipitates, after polishing, these two phases are distinguishable because of the different altitudes. The dark gray BCC precipitates distribute dispersedly in the bright FCC matrix. At the applied potential of 0.35 V vs. SCE, which locates above the E_b of the $Al_{0.5}CoCrFeNi$ alloy, localized corrosion has happened. As presented in Fig. 5d, the metal dissolution starts at the BCC phase and processes continually along the BCC precipitates nearby. As revealed in our previous research [22], the passive film formed on the Cr-depleted BCC phase is less protective than that formed on the FCC matrix, therefore, the easier breakdown of the passive film leads to the preferential dissolution of the BCC phase and the decreased breakdown potential.

Supplementary video related to this article can be found at https://doi.org/10.1016/j.jallcom.2020.156014

Fig. 6a shows the potentiodynamic-polarization curve of the $Al_{0.7}CoCrFeNi$ HEA. A stable passive region could be observed as well. The changes of the surface morphology during the polarization were captured in-situ and provided in the supplementary Video S3. Only one current fluctuation with the peak value of about

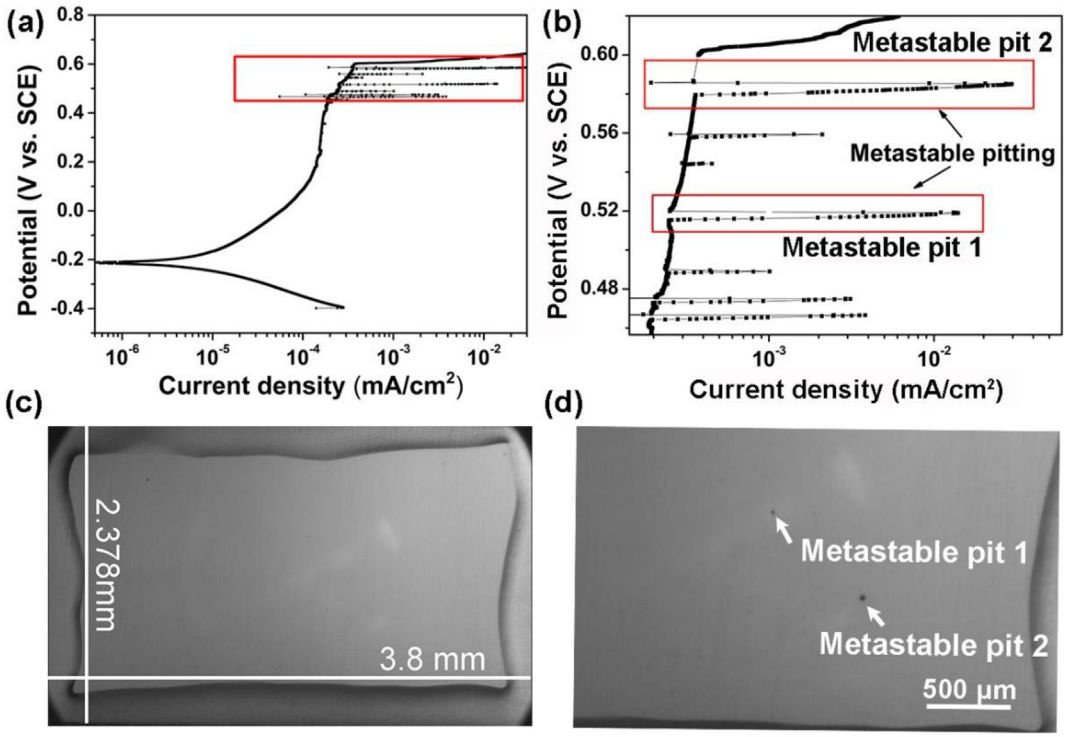

Fig. 4. Potentiodynamic-polarization curves and micrographs captured in-situ during the polarizations: (**a**) Potentiodynamic-polarization curve of the $Al_{0.3}CoCrFeNi$ HEA, with the scan rate of 1 mV/s in the 3.5 wt% NaCl solution at room temperature; (**b**) Enlarged current fluctuation of Fig. 4a; (**c**) Micrograph captured at OCP; (**d**) Micrograph captured at 0.6 V vs. SCE during the polarization test of Fig. 4a.

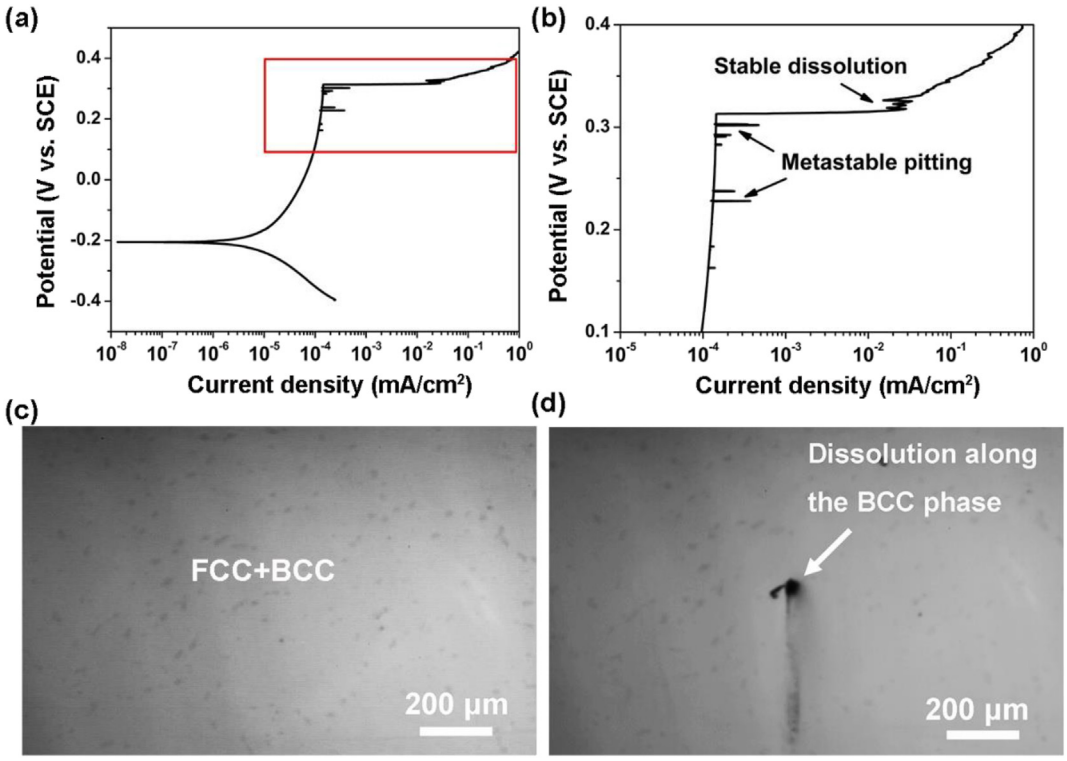

Fig. 5. Potentiodynamic-polarization curves and micrographs captured in-situ during the polarizations: (**a**) Potentiodynamic-polarization curve of the $Al_{0.5}$CoCrFeNi HEA, with the scan rate of 1 mV/s in the 3.5 wt% NaCl solution at room temperature; (**b**) enlarged current fluctuation of Fig. 5a; (**c**) micrograph captured at OCP; (**d**) micrograph captured at 0.35 V vs. SCE during the polarization test of Fig. 5a.

5×10^{-5} mA/cm^2 can be seen in the passive region (Fig. 6b). Similar to the $Al_{0.5}$CoCrFeNi alloy, because of the different mechanical properties between the FCC and BCC phase, the dendrite and interdendrite phases could be distinguished clearly under the visualization system at the OCP (Fig. 6c). After reaching the breakdown potential, a significant morphology change can be found, as shown in Fig. 6d, which micrograph is captured at 0.25 V vs. SCE. The localized corrosion initiates at the boundary between the FCC and BCC phases, propagate preferentially over the BCC interdendrite, and left the FCC phase unaffected.

Supplementary video related to this article can be found at https://doi.org/10.1016/j.jallcom.2020.156014

Ex-situ SEM observations of the surface morphology are conducted after polarizations. In $Al_{0.3}$CoCrFeNi alloy, the semi-sphere pit is observed, as presented in Fig. 7a. For the $Al_{0.5}$CoCrFeNi, as shown in Fig. 7b, the BCC precipitates are dissolved selectively. Fig. 7c indicates that localized corrosion occurs in the form of dissolution along the phase boundaries and dissolution of the BCC interdendrite. Overall, morphology changes of the Al_xCoCrFeNi ($x = 0.3, 0.5, 0.7$) HEAs observed by the in-situ visualization system during polarizations directly reveal the various corrosion processes in the Al_xCoCrFeNi HEAs. The localized corrosion mechanisms are different for the three HEAs under the influence of microstructure variation and chemical segregation.

4. Discussion

4.1. In-situ visualization of metastable pitting process

As the precursor of localized corrosion, metastable pitting plays an important role in the corrosion process. However, due to the limitation of observation method, the real-time metastable pitting process during the polarizations of HEAs remains unknown. In the present study, the metastable pitting processes of the $Al_{0.3}$CoCrFeNi HEA are firstly revealed in-situ by the advanced visualization system coupled with electrochemical polarization. As described in Section 3.3, the formation of the marked two pits in Fig. 4d can correspond to the current serrations marked in Fig. 4b (metastable pits 1 and 2) according to the in-situ observation. Fig. 8a plots the current density against time to show the evolution of the current transients of the metastable pit 1 and 2 during the polarization. All the current peaks show a slow rise and sudden decay in the present test. In previous studies, two types of anodic current transient have been observed. The Type I is distinguished by a slow growth of the current followed by a sudden cease of pit propagation [23]. On the contrary, Type II displays a rapid growth of the current, followed by a smooth decrease [24]. Some researchers considered that the current transients of each type are characteristic of a particular class of the metal. For instance, the Type I current transient is considered to be characteristic of metastable pitting in stainless steels of various types, whilst Type II is related to metastable pitting of pure Ion, carbon steel, or steels in which the Cr content is blow the limit of stainlessness [25]. Other authors [26] assumed that the two types of current transients represent two distinct processes before the formation of the stable pit, which are pit nucleation and metastable pit propagation. When a pit is nucleated, the current rises sharply above the background current, then decays continuously and slowly to the background level. Therefore, the current transient of Type II indicates the pit nucleation. The current transient caused by metastable propagation is characterized by a slowly rising current caused by the anodic dissolution of the inside surface of the pit during the metastable growth. Then after the brief period of propagation, the current suddenly decays when repassivation happen. Therefore, the Type I current transient represents the

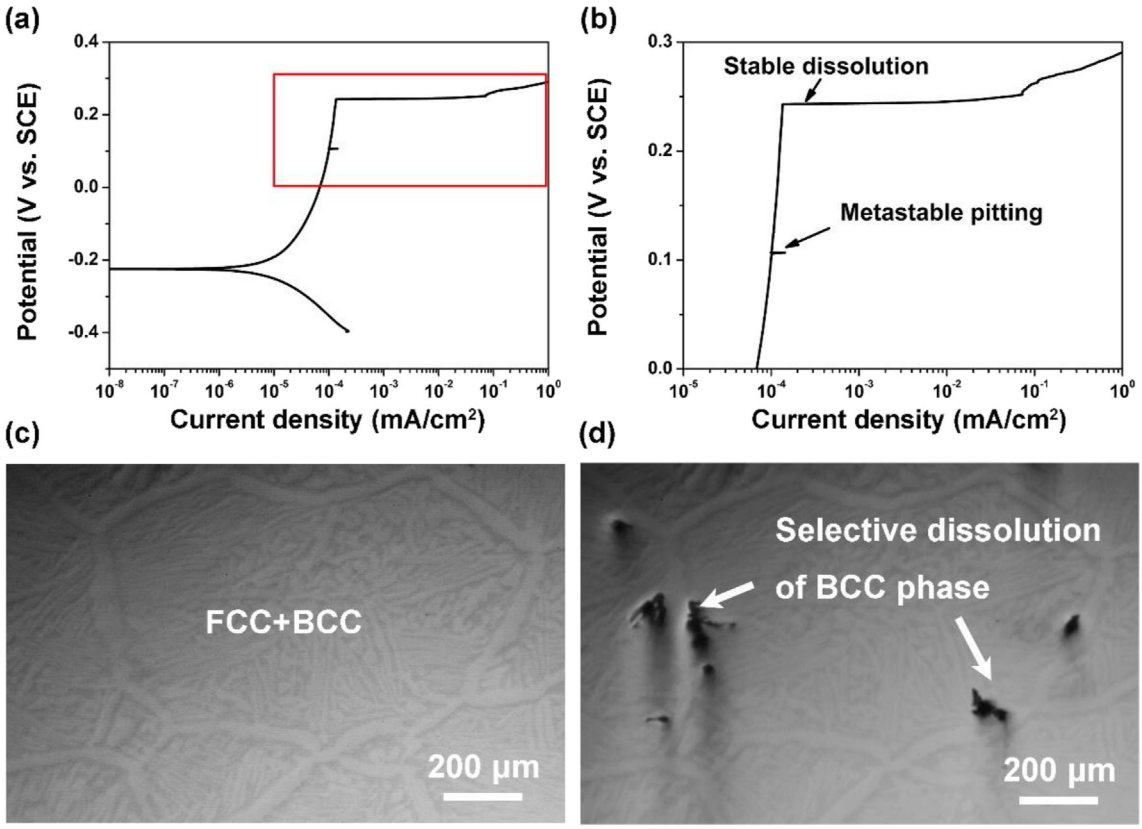

Fig. 6. Potentiodynamic-polarization curves and micrographs captured in-situ during the polarizations: (**a**) Potentiodynamic-polarization curve of the $Al_{0.7}CoCrFeNi$ HEA, with the scan rate of 1 mV/s in the 3.5 wt% NaCl solution at room temperature; (**b**) Enlarged current fluctuation of Fig. 6a; (**c**) Micrograph captured at OCP; (**d**) Micrograph captured at 0.25 V vs. SCE during the polarization test of Fig. 6a.

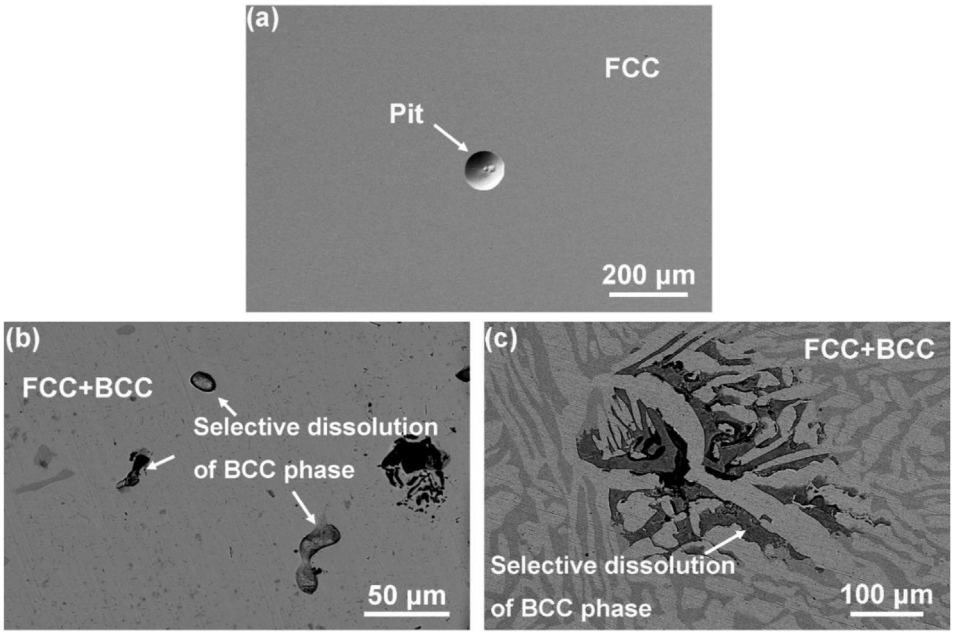

Fig. 7. Ex-situ SEM observation of the surface of the (a) $Al_{0.3}CoCrFeNi$, (b) $Al_{0.5}CoCrFeNi$, and (c) $Al_{0.7}CoCrFeNi$ HEAs after polarizaiton in the 3.5 wt% NaCl solution.

metastable pit processing [27,28]. In the present test, the current spikes show a typical shape of the Type I current transient during polarization, as can be seen in Fig. 8a, representing the formation and repassivation processes of the metastable pit in the $Al_{0.3}CoCrFeNi$ HEA.

As exhibited in Fig. 8a, the general trend of the current is

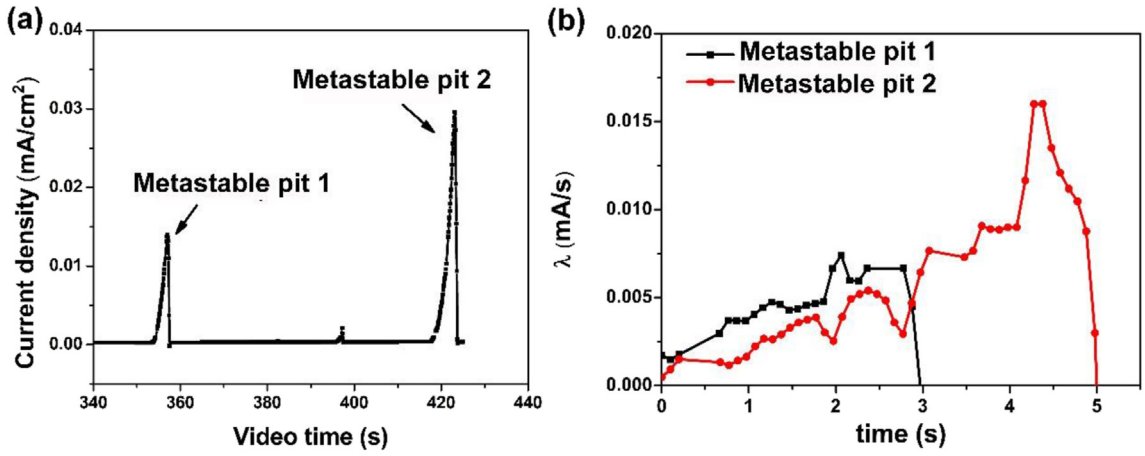

Fig. 8. (a) Plots of the current density against time to show the evolution of the current transients of the metastable pits; (b) Growth rate, λ, of the metastable pit generated on the $Al_{0.3}CoCrFeNi$ HEA electrode in the 3.5 wt % NaCl solution during potentiodynamic-polarizations.

approximately proportional to the square of time, indicating that metastable pit growth might be controlled by the diffusion of corrosion products [26,27]. To reveal the metastable pitting process furthermore, the slope, λ, of the rising part of a current spike, which characterizes the growth speed of a pit is plotted against time and shown in Fig. 7b. The λ is given by:

$$\lambda = \frac{I_n - I_{n-1}}{t_n - t_{n-1}} \quad (1)$$

where $n \geq 1$, I is the pitting current of a single pit, and t is the growth time of a pit. The λ value can be obtained by taking the first derivative of I with respect to t. Fig. 8b shows the λ values of the metastable pits 1, 2 marked in Fig. 4b. Although the lifetimes are different, the developments of the λ values have the similar trend. During the metastable pit growth, the general linear relationship between the λ and the time indicates that the metastable pitting process is diffusion controlled [29]. To be noticed, the potentiostatic-polarization was commonly used in the previous study of metastable pitting instead of potentiodynamic-polarization in the present study. However, as stated by Pistorius and Burstein [28], the current density in a single metastably-growing pit is independent of the applied potential, and the diffusion control allows no direct effect of the potential on pit growth. From Fig. 8b, the fluctuations of the λ value are common during the propagation process, which indicates that the metal dissolution during pit metastable growth is not stable. The activation and passivation occurred alternatively depends on the local anolyte condition in the pit. To be noticed, for the marked metastable pits 2, which have relatively longer lifetimes, before the repassivation (sharp decrease of the λ value), the λ increases suddenly in a very short period (about 0.5 s). This phenomenon indicates that the metal dissolution at the end of the metastable pit propagation is an accelerated process. The unstable metastable pit propagation is influenced by formation and rupture of the cover over the pit mouth, which process would be approved directly by the geometry changes of the marked metastable pit 2 observed by the in-situ visualization system.

The current serration and the corresponding in-situ observation of the metastable pit 2 are shown in the supplementary Video S4. Fig. 9 shows the in-situ photographs of the metastable pit 2 during the polarization. The surface morphologies were captured by cutting the video, and the photographs in Fig. 9 were selected with 0.5 s interval as examples to show the pit-morphological evolution. The real-time changes of the radius of the observed pit 2 were measured through the photographs with an interval of 0.25 s, and the results are exhibited in Fig. 10 (the red line). The radius of the pit can also be calculated through the pitting current transient. Based on the notion that the metal dissolution quantity is proportional to the change quantity as follows:

Supplementary video related to this article can be found at https://doi.org/10.1016/j.jallcom.2020.156014

Overall, during the potentiodynamic polarization of the $Al_{0.3}CoCrFeNi$ alloy, the metastable pit ceases as a consequence of the collapse of the pit cover. The real value of the pit mouth radius for the covered pit would be less before the cover collapsed. After the cover collapse, the measured pit radius would increase to reach and even exceed the calculated one, assuming an open hemispherical geometry. Repassivation would happen if the diluted anolyte in the pit cannot sustain the continual metal dissolution. If the pit has grown sufficiently for its own depth to act as the diffusion barrier before the complete rupture of the pit cover, the transition of the metastable pit to a stable one would occur.

4.2. Localized corrosion process

The in-situ visualization provides the direct information of the localized corrosion processes of the $Al_xCoCrFeNi$ HEAs during polarizations, which is useful for understanding the influence of microstructure and chemical segregation on the corrosion behavior. Due to the high-entropy effect, HEAs could form a supersaturated solid solution with one or more corrosion resistant elements. In the $Al_xCoCrFeNi$ HEAs, the formation of stable passive films enables the corrosion-resistant property. In particular, the high concentration of Cr, which possesses a high affinity to oxygen and a high chemical stability in the oxidized state [31], promotes the resistance of the protective passive film. However, with the increased Al content, the microstructure changes from the single FCC solid solution to FCC + BCC phases. The FCC phase is (Cr, Co, Fe)-rich, while the BCC phase is (Al, Ni)-rich. According to our previous study, the passive film formed on the Al-rich phase contains a higher fraction of the Al oxides/hydroxides, leading to the decrease of the compactness and corrosion-resistant ability [17]. The passive films that form on the Al-rich phases become the weak points preferentially attacked by Cl^- during anodic polarization. Therefore, the changes of microstructure from homogeneous to heterogeneous with chemical segregations would greatly influence the corrosion behavior, which are revealed by the local morphology

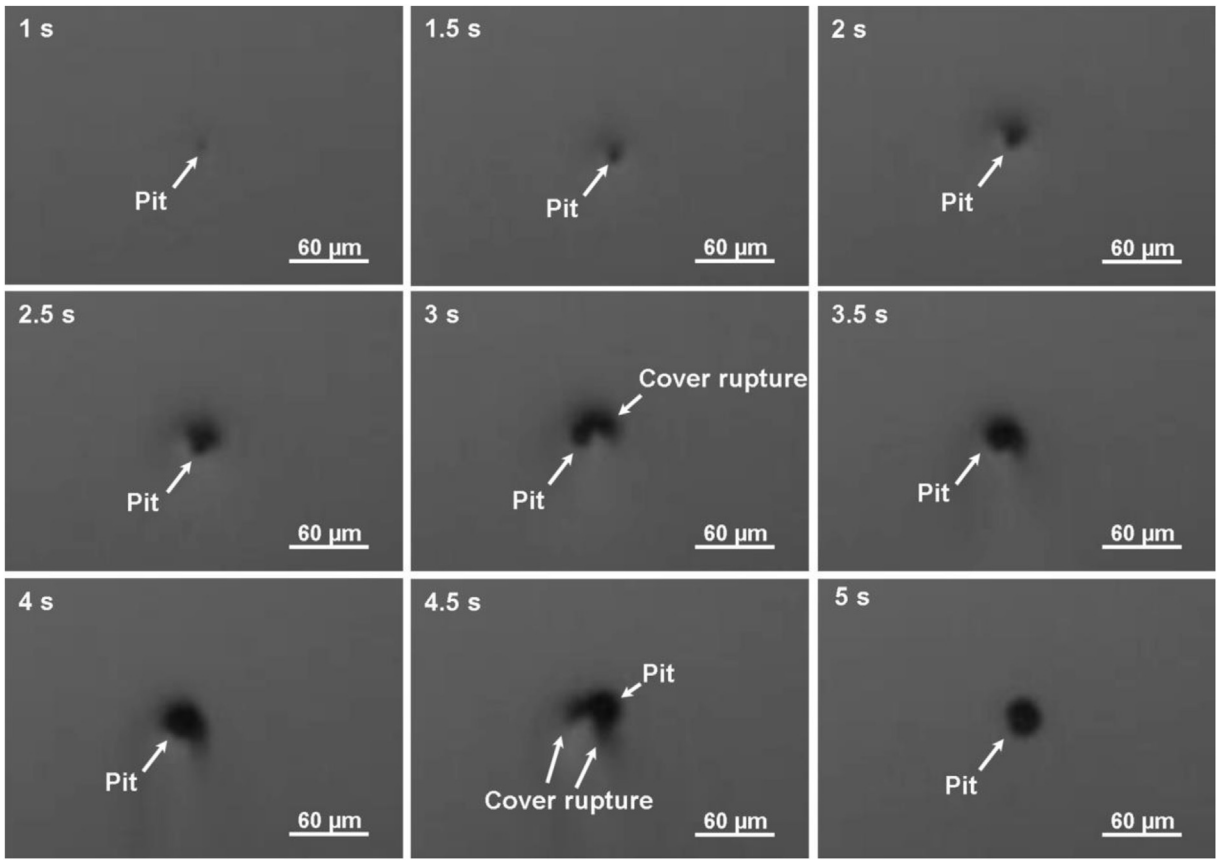

Fig. 9. In-situ growth images of the observed metastable pit 2 with the growth time from 1 to 5 s generated on the $Al_{0.3}CoCrFeNi$ HEA electrode in the 3.5 wt % NaCl solution during potentiodynamic polarization with the potential scan rate of 1 mV/s at room temperature.

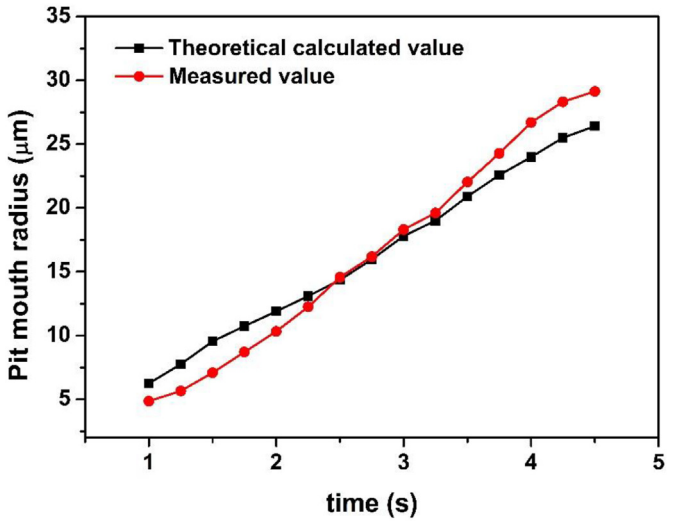

Fig. 10. Pit mouth radius (the theoretically-calculated and measured values) of the observed metastable pit 2 generated on the $Al_{0.3}CoCrFeNi$ HEA electrode in the 3.5 wt % NaCl solution during potentiodynamic polarization with the potential scan rate of 1 mV/s at room temperature.

changes during polarizations recorded by the in-situ visualization system.

As indicated by the in-situ visualization results, the uniform FCC $Al_{0.3}CoCrFeNi$ alloy possesses the best corrosion resistant ability. The breakdown of the passive film exhibits in the form of randomly distributed pits. The increase of the Al content leads to the appearance of Cr-depleted BCC phase in the $Al_{0.5}CoCrFeNi$ alloy. The preferential dissolution of the passive film formed on the BCC phase results in the initial localized corrosion. At the same time, the localized corrosion resistance becomes weak, indicated by the decreased E_b. With the further increase of Al content, the volume fraction of the BCC phase increases dramatically. No pit is observed in the $Al_{0.7}CoCrFeNi$ alloy. Localized corrosion occurs in the form of etching along the phase boundaries and the selective dissolution of the BCC interdendrites. The E_b decreases furthermore. Overall, the local morphology changes detected by the in-situ visualization system during polarizations reveal different localized corrosion processes of $Al_xCoCrFeNi$ HEAs. With the microstructure changes from single phase to multi-phases, the dominated form of localized corrosion changes form pitting to selectively dissolution of BCC phase, leading to the decreased corrosion resistance.

5. Conclusions

The localized corrosion mechanism and metastable pitting process of the $Al_xCoCrFeNi$ ($x = 0.3$, 0.5, and 0.7) HEAs are revealed in-situ by an advanced visualization system coupled with electrochemical polarization. Features of the surface could be monitored on both micro-spatial and temporal scales during polarization. The present study elaborates the influence of microstructure and chemical segregation on localized corrosion. In addition, the in-situ visualization uncovers the evolution of metastable pitting process of the $Al_{0.3}CoCrFeNi$ alloy. The main conclusions could be drawn as follows.

(1) The $Al_{0.3}$CoCrFeNi alloy possesses a single FCC solid solution with elements homogeneously distributed. With the increased aluminum content, $Al_{0.5}$CoCrFeNi and $Al_{0.7}$CoCrFeNi alloys consist of FCC and BCC phases. The multi-phase microstructure leads to the elemental segregation. The FCC phase is (Cr, Co, Fe)-rich, while the BCC phase is (Al, Ni)-rich.
(2) In the single FCC phase $Al_{0.3}$CoCrFeNi HEA, localized corrosion shows in the form of pitting. In the $Al_{0.5}$CoCrFeNi and $Al_{0.7}$CoCrFeNi alloys, the localized corrosion initiates and propagates in the Cr-depleted BCC phase. The dominated form of localized corrosion changes form pitting to selectively dissolution of BCC phase, leading to the decreased corrosion resistance.
(3) The current serrations observed during the polarization test of the $Al_{0.3}$CoCrFeNi HEA, which show a typical slow rise and sudden decay, represent the formation and repassivation processes of metastable pits. The metastable pit growth is diffusion controlled. The metal dissolution during pit growth is not stable as proved by the pit configuration changes. The rupture of the pit cover leads to the openness of the pit, and promotes the repassivation.

CRediT authorship contribution statement

Yunzhu Shi: Conceptualization, Methodology, Investigation, Writing - original draft. **Jingke Mo:** Software, Investigation. **Feng-Yuan Zhang:** Resources. **Bin Yang:** Writing - review & editing. **Peter K. Liaw:** Conceptualization, Supervision. **Ying Zhao:** Supervision, Writing - review & editing.

Declaration of competing interest

The authors declare that they have no known competing financial interests or personal relationships that could have appeared to influence the work reported in this paper.

Acknowledgement

This work was supported by Shenzhen Science and Technology Research Funding [JCYJ20160608153641020], National Natural Science Foundation of China [No. 51901242], China Postdoctoral Science Foundation [No. 2018M643247], U.S. Department of Energy, Office of Fossil Energy, National Energy Technology Laboratory [DE-FE-0008855, DE-FE-0024054, and DE-FE-0011194], National Science Foundation [DMR-1611180 and 1809640], and Beijing Municipal Natural Science Foundation [No. 2162026].

References

[1] J.W. Yeh, S.K. Chen, S.J. Lin, J.Y. Gan, T.S. Chin, T.T. Shun, C.H. Tsau, S.Y. Chang, Nanostructured high-entropy alloys with multiple principal elements: novel alloy design concepts and outcomes, Adv. Eng. Mater. 6 (2004) 299–303.
[2] B. Cantor, I.T.H. Chang, P. Knight, A.J.B. Vincent, Microstructural development in equiatomic multicomponent alloys, Mater. Sci. Eng. 375–377 (2004) 213–218.
[3] Y. Zhang, T.T. Zuo, Z. Tang, M.C. Gao, K.A. Dahmen, P.K. Liaw, Z.P. Lu, Microstructures and properties of high-entropy alloys, Prog. Mater. Sci. 61 (2014) 1–93.
[4] M.C. Gao, Chapter 11: design of high-entropy alloys, in: M.C. Gao, J.W. Yeh, P.K. Liaw, Y. Zhang (Eds.), High-entropy Alloys: Fundamentals and Applications, Springer, Cham, Switzerland, 2016.
[5] M.C. Gao, B. Zhang, S.M. Guo, J.W. Qiao, J.A. Hawk, High-entropy alloys in hexagonal close-packed structure, Metall. Mater. Trans. 47 (2015) 3322–3332.
[6] Y. Zhang, Y.J. Zhou, J.P. Lin, G.L. Chen, P.K. Liaw, Solid-solution phase formation rules for multi-component alloys, Adv. Eng. Mater. 10 (2008) 534–538.
[7] K.M. Youssef, A.J. Zaddach, C. Niu, D.L. Irving, C.C. Koch, A novel low-density, high-hardness, high-entropy alloy with close-packed single-phase nanocrystalline structures, Materials Research Letters 3 (2015) 95–99.
[8] Z. Li, K.G. Pradeep, Y. Deng, D. Raabe, C.C. Tasan, Metastable high-entropy dual-phase alloys overcome the strength–ductility trade-off, Nature 534 (2016) 227–230.
[9] X. Lim, Mixed-up metals make for stronger, tougher, stretchier alloys, Nature 533 (2016) 306–307.
[10] R. Sriharitha, B.S. Murty, R.S. Kottada, Alloying, thermal stability and strengthening in spark plasma sintered AlxCoCrCuFeNi high entropy alloys, J. Alloys Compd. 583 (2014) 419–426.
[11] M.-H. Chuang, M.-H. Tsai, W.-R. Wang, S.-J. Lin, J.-W. Yeh, Microstructure and wear behavior of AlxCo1.5CrFeNi1.5Tiy high-entropy alloys, Acta Mater. 59 (2011) 6308–6317.
[12] Y. Shi, B. Yang, P.K. Liaw, Corrosion-resistant high-entropy alloys: a review, Metals 7 (2017) 43.
[13] Z. Tang, M.C. Gao, H. Diao, T. Yang, J. Liu, T. Zuo, Y. Zhang, Z. Lu, Y. Chen, Y. Zhang, K.A. Dahmen, P.K. Liaw, T. Egami, Aluminum alloying effects on lattice types, microstructures, and mechanical behavior of high-entropy alloys systems, J. Occup. Med. 65 (2013) 1848–1858.
[14] Z. Tang, L. Huang, W. He, P.K. Liaw, Alloying and processing effects on the aqueous corrosion behavior of high-entropy alloys, Entropy 16 (2014) 895–911.
[15] Q.H. Li, T.M. Yue, Z.N. Guo, X. Lin, Microstructure and corrosion properties of AlCoCrFeNi high entropy alloy coatings deposited on AISI 1045 steel by the electrospark process, Metall. Mater. Trans. 44 (2012) 1767–1778.
[16] J. Li, X. Yang, R. Zhu, Y. Zhang, Corrosion and serration behaviors of TiZr0.5NbCr0.5VxMoy high entropy alloys in aqueous environments, Metals 4 (2014) 597–608.
[17] Y. Shi, B. Yang, X. Xie, J. Brechtl, K.A. Dahmen, P.K. Liaw, Corrosion of Al xCoCrFeNi high-entropy alloys: Al-content and potential scan-rate dependent pitting behavior, Corrosion Sci. 119 (2017) 33–45.
[18] J. Mo, Z. Kang, S.T. Retterer, D.A. Cullen, T.J. Toops, J.B. Green Jr., M.M. Mench, F.-Y. Zhang, Discovery of true electrochemical reactions for ultrahigh catalyst mass activity in water splitting, Science Advances 2 (2016), e1600690.
[19] J. Mo, Z. Kang, G. Yang, Y. Li, S.T. Retterer, D.A. Cullen, T.J. Toops, G. Bender, B.S. Pivovar, J.B. Green Jr., F.-Y. Zhang, In situ investigation on ultrafast oxygen evolution reactions of water splitting in proton exchange membrane electrolyzer cells, J. Mater. Chem. 5 (2017) 18469–18475.
[20] Z. Kang, J. Mo, G. Yang, S.T. Retterer, D.A. Cullen, T.J. Toops, J.B. Green Jr., M.M. Mench, F.-Y. Zhang, Investigation of thin/well-tunable liquid/gas diffusion layers exhibiting superior multifunctional performance in low-temperature electrolytic water splitting, Energy Environ. Sci. 10 (2017) 166–175.
[21] W. Tian, N. Du, S. Li, S. Chen, Q. Wu, Metastable pitting corrosion of 304 stainless steel in 3.5% NaCl solution, Corrosion Sci. 85 (2014) 372–379.
[22] Y. Shi, L. Collins, R. Feng, C. Zhang, N. Balke, P.K. Liaw, B. Yang, Homogenization of AlxCoCrFeNi high-entropy alloys with improved corrosion resistance, Corrosion Sci. 133 (2018) 120–131.
[23] G.T. Burstein, C. Liu, R.M. Souto, S.P. Vines, Origins of pitting corrosion, Corrosion Eng. Sci. Technol. 39 (2004) 25–30.
[24] S.T. Pride, J.R. Scully, J.L. Hudson, Metastable pitting of aluminum and criteria for the transition to stable pit growth, J. Electrochem. Soc. 141 (1994) 3028–3040.
[25] J. Soltis, Passivity breakdown, pit initiation and propagation of pits in metallic materials – Review, Corrosion Sci. 90 (2015) 5–22.
[26] G.T. Burstein, C. Liu, R.M. Souto, S.P. Vines, Origins of pitting corrosion, Corrosion Eng. Sci. Technol. 39 (2004) 25–30.
[27] P.C. Pistorius, G.T. Burstein, Metastable pitting corrosion of stainless steel and the transition to stability, Philos. Trans. R. Soc. 341 (1992) 531–559.
[28] G.T. Burstein, S.P. Mattin, Nucleation of corrosion pits on stainless steel, Phil. Mag. Lett. 66 (2006) 127–131.
[29] D.E. Williams, J. Stewart, P.H. Balkwill, The nucleation, growth and stability of micropits in stainless steel, Corrosion Sci. 36 (1994) 1213–1235.
[30] N.J. Laycock, R.C. Newman, Localized dissolution kinetics, salt films and pitting potentials, Corrosion Sci. 39 (1997) 1771–1790.
[31] Z.H. Jin, H.H. Ge, W.W. Lin, Y.W. Zong, S.J. Liu, J.M. Shi, Corrosion behaviour of 316L stainless steel and anti-corrosion materials in a high acidified chloride solution, Appl. Surf. Sci. 322 (2014) 47–56.